analytical chemistry

Article

pubs.acs.org/ac

Pressure-Driven Chromatographic Separation Modes in Self-Enclosed Integrated Nanocapillaries

Lian Duan,[†] Zhen Cao,[†] and Levent Yobas*[,†,‡]

[†]Department of Electronic and Computer Engineering and [‡]Division of Biomedical Engineering, The Hong Kong University of Science and Technology, Clear Water Bay, Hong Kong SAR, China

Supporting Information

ABSTRACT: This study presents pressure-driven chromatographic separation characteristics of integrated nanofluidic channels (nanocapillaries) featuring distinct cross-sectional geometries: cylindrical, triangular, and rectangular profiles. Cylindrical and triangular nanocapillaries are self-enclosed robust conduits realized through standard semiconductor processing techniques using low-resolution photolithography. Specifically, capillaries in nominal radius 300 and 500 nm have been investigated for chromatographic separation in comparison to 750 nm deep nanoslits as well as triangular capillaries featuring an inscribed circle about 500 nm in radius. Chromatograms have been obtained from 10 mm long nanocapillaries under various modes: normal- and reversed-phase, ion-valence, and hydrodynamic chromatography. The van Deemter plots based on the linear mobile phase velocity for 300 nm radius capillaries and 750 nm deep slits show excellent agreement with the plate heights theoretically predicted. The minimum plate heights achieved are typically below 2 μm and the theoretical plate numbers are in the order of 10^5 plates/m for the most chromatography modes investigated in the pressure range up to 100 psi. A comparatively high resolving power is achieved with cylindrical nanocapillaries especially those 300 nm in radius. Self-enclosed robust nanocapillaries demonstrated here could facilitate a pressure-driven chromatographic analysis of extremely low-volume samples (e.g., single cell).

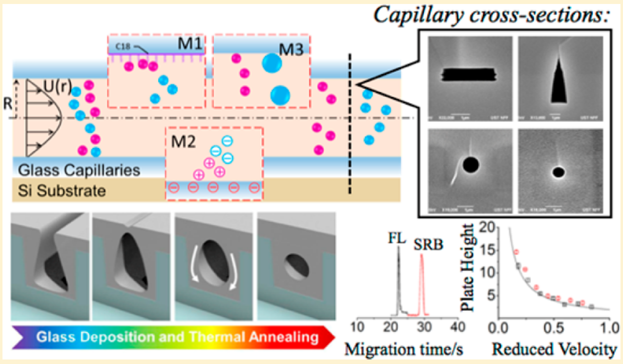

Nanofluidic channels, nanochannels or nanocapillaries with hydraulic diameter in the range of $10^1 - 10^3$ nm, a length scale dubbed as "extended nanospace", are of significance in separation science for chemical and biological analysis.[1,2] Such small scales substantially reduces the requirement of sample and reagent consumption, a feature that could not only lead to cost savings but also facilitate single-cell analytics.[3] Moreover, as the surface effects in nanochannels take over bulk phenomena, unique features emerge with the channel content displaying altered physical properties in relation to bulk fluid; increased viscosity and reduced dielectric constant,[4] as well as enhanced proton mobility.[5] Notable phenomena discovered in such confined spaces include the enrichment and depletion of ions,[6] reduced electro-osmotic flow,[7] rapid current decrease,[8] and peculiar meniscus shape.[9]

Separation in miniaturized systems has been extensively studied using electrokinetic means as opposed to pressure-driven flows because of the complexities involved with pumping pressure, fluidic plumbing, and connections, which become aggravated with further miniaturization. A few studies have taken advantage of the extended nanospace and demonstrated gel-free electrophoresis of DNA and proteins. Han and co-workers achieved this via periodic arrangements of deep and shallow nanoslits featuring entropic traps.[10] Peterson et al., showed that DNA could be separated in nanoslits of a uniform depth by using the parabolic electroosmotic flow profile under overlapped electrical double layers (EDLs).[11] Pennathur and Santiago further investigated the underlying mechanism using channels 40−1560 nm deep.[12] The authors also investigated the electromigration of neutral and charged species in nanochannels and described a new electrokinetic separation mechanism by ion valences (EKSIV), a technique where the separation of small analyte ions are strongly influenced by the transverse electric fields associated with finite EDLs.[13,14] Garcia et al., similarly noticed in silica nanochannels faster migration rates for anionic species than those neutral toward the cathode.[15] Subsequently, Griffiths and Nilson, using numerical methods, examined the transport of charged species in nanochannels with a width comparable to the EDL thickness.[16] Xuan and Li derived governing equations and theoretically compared the separation efficiency to that in a pressure-driven nanochannel flow.[17,18]

The pressure-driven separation methods can accommodate organic solvents as well as aqueous solvents over a broad pH range and thus are less restricting than the electrokinetic methods for implementing various chromatography modes. Liquid chromatography (LC) is one of the most popular

Received: August 9, 2016
Accepted: November 1, 2016
Published: November 1, 2016

DOI: 10.1021/acs.analchem.6b03094
Anal. Chem. 2016, 88, 11601−11608

methods and yet its miniaturization has faced the challenge of securing uniformly packed columns in microfluidic channels. Tallarek and co-workers investigated particulate packing for various channel geometries.[19] He and Regnier addressed the packing by introducing collocated monolith support structures (COMOSS) lithographically etched into channels.[20] A further alternative to the uniformly packed particulates is open tubular columns with the stationary phase located on the tubing walls. Yet, such columns require a tubing radius of less than 1 μm to avoid the rate-limited mobile-phase mass transfer.[21] Although this requirement is readily met by the extended nanospace, only a handful studies attempted pressure-driven open-tubular LC in nanofluidic channels probably due to their excessive fluidic resistance and sophisticated fabrication. Liu and colleagues used pressure-driven fused-silica bare nanocapillaries and resolved ionic dyes, proteins, and DNA strands at a broad size range through hydrodynamic chromatography and chromatography based on non-negligible EDLs.[22−24] Kitamori and colleagues further scaled the sample injection volume down to atto- to femtoliters by fabricating a glass microchip with channels in width and depth limited to a few hundred nanometers; the authors demonstrated pressure-driven separation of ionic dyes in an aqueous mobile phase as well as fluorescent dyes in a nonpolar mobile phase.[25,26]

Integrated nanochannels as opposed to discrete fused-silica nanocapillaries could lead to a microsystem wherein various functional units (e.g., for single cell trapping, lysis, and analysis) are brought together with minimal dead volume. The integration allows further miniaturization as well. However, the process often involves etching a silica-based substrate that is patterned via advanced tools (e.g., e-beam lithography), which are fairly low throughput and costly. More importantly, such a process is unable to emulate the desired structure and surface finish of the fused-silica capillaries that are heat drawn. A further issue deals with obtaining effectively sealed silica nanochannels that can sustain high-pressure chromatography.[27] Bypassing all these issues could lead to nanochannels with desired attributes for a variety of applications, including pressure-driven chromatography for which the characteristics of such integrated nanochannels have yet to be revealed.

Here, we demonstrate integrated nanocapillaries distinct from those known nanochannels in structure as well as fabrication process and present their characteristics for various LC modes. The nanocapillaries have several notable merits. First, their structure is of a self-enclosed glass conduit on silicon; they are robust against high pressure in comparison to those formed by bonding substrates together. Second, their fabrication requires standard semiconductor processing techniques and low-resolution photolithography; they are amenable to mass production and large-scale integration to tap on economies of scale for commercialization. Third, their interior has a cylindrical profile within a monolithic glass layer, defined by thermal reflow (Figure 1a);[28] they offer a smooth and stable surface featuring comparatively homogeneous EDLs, as opposed to those formed by various etch techniques and bonding dissimilar materials, and also the functionalization of which is relatively well understood. Fourth, their diameter remains longitudinally uniform and controllably scales below 100 nm through extended reflow;[28] they do not require low-throughput costly patterning tools.

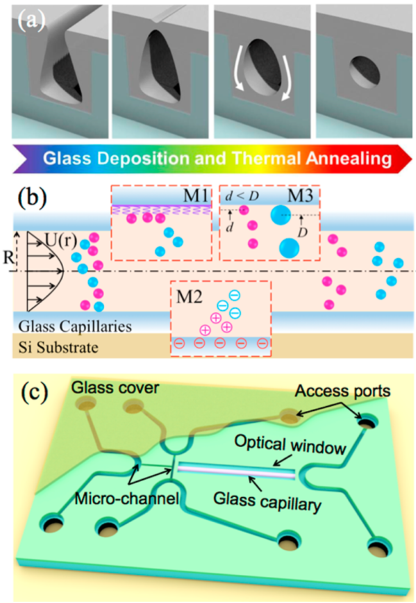

Figure 1. Illustrations: (a) integration concept of the self-enclosed nanocapillaries; (b) pressure-driven chromatography modes addressed here; and (c) 3D device rendering. (a) Arrows denote thermal reflow of the glass layer under the surface tension forces. (b) Binary mixture of species is subjected to pressure-driven parabolic velocity profile, undergoing separation along the integrated glass nanocapillary according to the chromatography modes (insets): M1 polar/nonpolar interactions; M2 charge-based interactions; and M3 hydrodynamic chromatography.

We previously demonstrated such nanocapillary segments for gel-free electrophoresis of proteins and DNA fragments.[29,30] Although proven to be effective, the required high driving voltages subsequently led to electric-field-induced aggregates.[31] This has motivated the present study where we investigated nanocapillaries in radius 500 and 300 nm and length 10 mm for the pressure-driven chromatography modes (Figure 1b). We also tested self-enclosed glass capillaries in triangular cross-sectional profile (those that skipped thermal reflow) and conventional nanochannels (750 nm deep rectangular nano-slits), all sharing the same layout.

■ EXPERIMENTAL SECTION

Fabrication. Figure 1a describes the integration concept. For details, see text and Figure S-1 in Supporting Information. A thick layer of doped glass gets deposited at a nonconformal thickness profile, leaving a trapped void elongated inside a silicon trench as a precursor of self-enclosed nanocapillary. The void initially projects a triangular cross-sectional profile. Subsequent shape transformation through annealing turns the void into a cylindrical tube with the surrounding doped glass layer undergoing thermal reflow as a result of the surface tension forces across the glass layer. Extended annealing controllably shrinks the capillary diameter into the realm of the extended nanospace. The nanocapillaries are integrated with a sample injection junction and a set of microfluidic delivery channels enclosed under a glass cover (Figure 1c).

Coating. The coating procedure is according to ref 32. The devices were rinsed with methanol pumped in at 60 psi for 3 h and then with HPLC-grade toluene at 40 psi for 5 h. The toluene was dried a priori over a 3 Å molecular sieve for more than 12 h. Subsequently, the devices were presented with the coating solution pumped in at 20 psi for 12 h and contained trimethoxy-(octadecyl)-silane mixed with dry toluene at a ratio of 10:90 (v/v) with a freshly added 0.5% triethylamine as the catalyst. Residual coating solution was removed by pumping in the toluene at 40 psi for 5 h and then the methanol at 60 psi for 3 h. All the solutions were collected from the separation waste port. The devices were filled with the aqueous phase and preserved in water bath until experiments.

Reagents. Fluorescein, sulforhodamine B, rhodamine B, pyrromethene 597, coumarin 460, and sodium tetraborate were all acquired from Aldrich (Milwaukee, WI); fluorescein-5-isothiocyanate (FITC), glutamic acid (Glu), serine (Ser), and leucine (Leu) from Sigma Chemicals Co. (St. Louis, MO); arginine monohydrochloride (Arg), alanine (Ala), proline (Pro), phenylalanine (Phe), valine (Val), and sodium perchlorate from Sigma-Aldrich (St. Louis, MO); ethanol absolute and acetonitrile both gradient grade from Merck (Kenilworth, NJ); sodium citrate buffer from Fluka (Ronkonkoma, NY); and toluene and methanol from VWR (Radnor, PA). Cy3-labeled SET8 protein was kindly provided by Prof. Hyokeun Park.

In chromatographic modes, the running buffer (the mobile phase) was composed of either a mixture of toluene and the ethanol absolute at a ratio 99:1 (v/v) or 100 μM borax solution (sodium tetraborate dissolved in ultrapure deionized (DI) water, pH, 8.9), or 10 mM citrate buffer (pH 5.5) with 10 mM sodium perchlorate and acetonitrile (12 or 25%), or 1× phosphate-buffered saline (PBS) solution (composition all in mM: 137 NaCl, 2.7 KCl, 10 Na_2HPO_4, and 1.8 KH_2PO_4). The pH was adjusted by adding H_3PO_4 or NaOH and measured with a pH meter (Mettler Toledo, Inc., OH). Pyrromethene 597 (10 μM), coumarin 460 (100 μM), fluorescein (20 μM), sulforhodamine B (5 μM), Arg, and Glu (both 100 μM), and the remaining amino acids (5 mM) were dissolved in their respective running buffers and then test mixtures were prepared for the device characterization. Rhodamine B (2 μM) was individually run in the borax solution as the velocity indicator. For labeling, all the amino acids were mixed with 1 mM FITC solution (10 mg FITC in 25 mL acetone) at a ratio 100:1 (v/v) and then incubated in the dark overnight. Protein SET8 was labeled with Cy3 according to the instructions of the Amersham Cy3 Ab Labeling Kit (GE Healthcare, NJ, U.S.A.). The chemicals were dissolved with DI water and adjusted to pH ∼ 7.4.

Measurements. All the experiments were observed under an epifluorescence microscope (Eclipse, Nikon, Tokyo, Japan) equipped with a mercury lamp (100 W) and a filter cube set for the excitation and detection of the fluorescent bands (ex/em all in nm: 495/519, FITC; 552/574, rhodamine B; 558/576, sulforhodamine B; 494/512 fluorescein; 512/570, Cy3; 462/512, C460; 532/565, P597). The time-series images of the fluorescent bands were captured by an EMCCD camera (iXon3 897, Andor Technology PLC, Northern Ireland, U.K.) through a 20× objective lens (Carl Zeiss, Oberkochen, Germany). The fluorescent intensities from a select region of interest (∼2 μm by 2 μm) were then analyzed through an image processing software (ImageJ; NIH, Bethesda, MD) and plotted against the time scale to generate the chromatograms. In the chromatograms, each peak was fitted with Gaussian to acquire the essential parameters, including the retention time, base width, and band variance (Origin 8.0, OriginLab Corp., Northampton, MA). For the fitted peaks, the theoretical plates were evaluated as $N = 16(t_R/w_b)^2$, where t_R is the retention time and w_b is the base width in units of time. The experimental plate heights were evaluated as $H = (\sigma_{det}^2 - \sigma_{inj}^2)/L_{eff}$, with L_{eff} being the effective separation length (50 μm short of the separation length stated as 6 or 10 mm), and σ_{inj}^2 and σ_{det}^2 the band variances at a distance 50 μm and L_{eff} from the injection points, respectively. The resolution between respective peaks was given by the difference in their retention time divided by their average width: $R_s = 2(t_{R,1} - t_{R,2})/(w_{b,1} + w_{b,2})$.

Sample Plug Injection. A "pinched-injection" scheme was adopted for the precision injection of a sample plug $\lesssim$200 fL into the nanocapillaries through a custom-built pneumatic system (Figure S-2) capable of switching the pressure supply at a temporal resolution of 10 ms (Supporting Information). Sample loading, injection, and plug formation were executed sequentially (Figure S-3a). The device was initially filled with a mobile phase. During sample loading, the sample and buffer ports were both pressurized at 40 psi and the buffer waste port at 60 psi, while the sample waste port being vent to the atmosphere. The sample injection was initiated and terminated by switching off the buffer waste port and then the sample port both to the atmosphere. The time elapsed between the two events (10 ms) determined the injected sample plug size (∼50 μm) as revealed by the chromatograms (Figure S-3b). Injection intervals below 100 ms led to a symmetric Gaussian plug profile because of the longitudinal dispersion whereas prolonged injection beyond 300 ms delivered an asymmetric plug profile featuring a steep rise and a gradual fall. In the experiments, we varied injection intervals to obtain an initial plug length of 100−150 μm to overcome inadequate detection sensitivity while achieving comparatively high separation efficiency.

■ RESULTS AND DISCUSSION

Nanocapillaries. Figure 2a depicts the sample injection cross-junction in optical and scanning electron microscopy (SEM) images. The self-enclosed capillaries (total 6) can be partially seen through the optical window etched into the a-Si layer. The capillaries extend further underneath the a-Si layer and join the sample injection cross-junction. The channel that delivers the sample runs orthogonal to the capillaries with its width and depth limited to 6 μm and extends 1 mm on either side of the junction before joining the U-shaped wider channels. The buffer is supplied by 1 mm long parallel channels (total 6) each 3 μm wide and 6 μm deep and aligned with the corresponding separation nanocapillary. The sample-injection cross-junction is nearly identical across all the devices, which mainly differed in their nanocapillaries radii or cross-sectional profiles (Figure 2b−e). In some devices, the self-enclosed capillaries were replaced, for benchmarking, with conventional channels in rectangular profile 2.7 μm wide and 750 nm deep (Figure 2b). In some other devices, the self-enclosed capillaries featured triangular profile 1.26 μm in base width and 3.4 μm in height (Figure 2c). For the remaining devices, the self-enclosed capillaries are in cylindrical profile with a nominal radius 500 and 300 nm as depicted in Figure 2d and e, respectively. These nominal values are representative of actual measurements, which show less than ∼3% variations across device or wafer (Table S-1).

Normal-Phase LC. Figure 3a shows chromatograms of coumarin 460 (C460) and pyrromethene 597 (P597) obtained with a nonpolar solvent (toluene) as the mobile phase and the silica walls of the conventional (nanoslit) and the self-enclosed nanochannels featuring polar silanol groups as the stationary phase. For each case, the reproducibility of the separation is established by overlaying three chromatographs obtained at an eluent pressure of 40 psi. P597, unlike C460, does not interact with silanol groups and hence exhibits a short retention time.

DOI: 10.1021/acs.analchem.6b03094
Anal. Chem. 2016, 88, 11601−11608

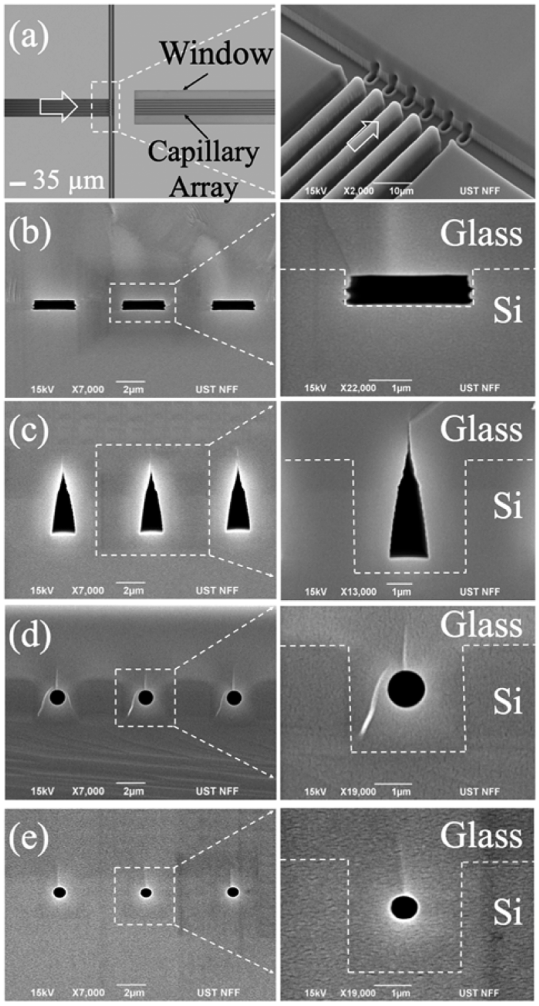

Figure 2. (a) Planar and oblique views of a sample injection cross-junction. (b−e) SEM images capturing the cross-sectional view of the integrated nanocapillaries featuring (b) rectangular, (c) triangular, and (d, e) cylindrical profile. Scale bars on the left panel (a) 35 μm and (b−e) 2 μm and on the right panel (a) 10 μm and (b−e) 1 μm.

This was also confirmed by the experiments with the mobile phase being adjusted to various polarity levels by diluting toluene with ethanol at an appropriate volume ratio (Figure S-4).

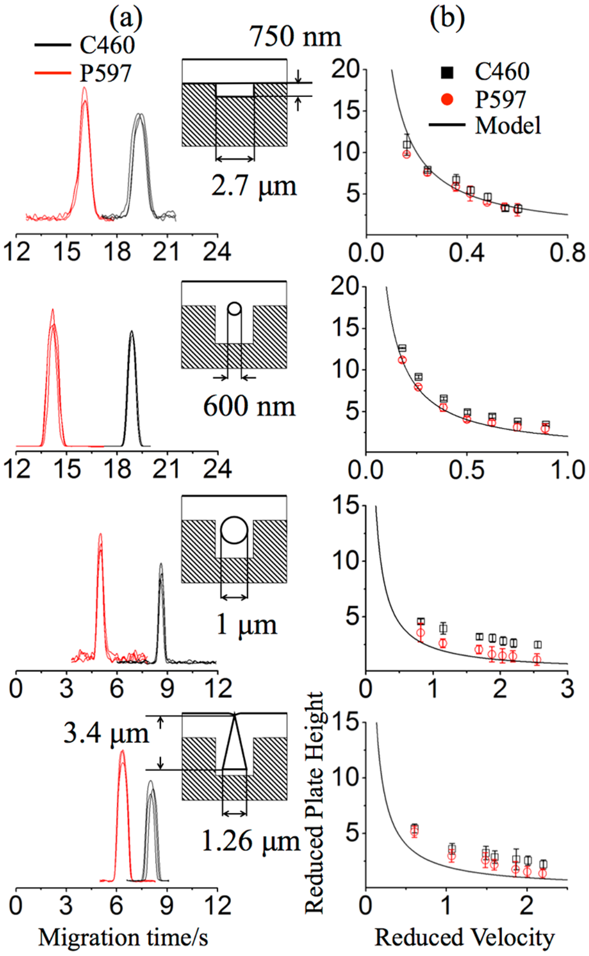

Figure 3. Normal-phase LC. (a) Overlaid chromatograms of C460 and P597 (3 repeats) in 99/1 (v/v) toluene/ethanol separated through nanoslits or self-enclosed nanocapillaries of respective cross-sectional profile (insets). (b) Corresponding reduced van Deemter curves. Error bars: ±1 s.d. (n = 5). The model lines describe $h = B/\upsilon + C\upsilon$, where B is 2 and C is 0.0476 for nanoslits and 0.0104 for triangular and cylindrical capillaries. Separation length and pressure: 10 mm; (a) 40 and (b) 20−100 psi.

The chromatograms from 750 nm deep rectangular channels (nanoslits) and 300 nm radius self-enclosed capillaries exhibit a similar residence time (∼20 s). However, the self-enclosed capillaries offer a higher resolution (R_s = 5.9) than the nanoslits (R_s = 3.2). While this attests the significance of the cylindrical profile, the effect of the diameter can be noticed in the separation results from 500 nm radius capillaries for which a comparable resolution is achieved (R_s = 5.4). Nevertheless, this comparison is confounded by the unequal residence times; one may argue that even higher resolution can be obtained from large capillaries by increasing the residence times to equal levels. While reducing the elution pressure across large capillaries could address this issue, the influence of the elution pressure on the resolution should not be ignored.[22] Instead, moving the detection zone upstream along narrow capillaries while maintaining the same pressure level yields comparable residence times, which occurs at a separation length of 6 mm and returns a slightly increased resolution (R_s = 6.2, Figure S-5a). This outcome is reasonable because mass transfer and surface interactions get enhanced in narrow capillaries. Although the capillary diameter can be further scaled below 100 nm through thermal reflow,[30] narrower capillaries were avoided due to the inadequate detection limit of our experimental setup. The self-enclosed nanocapillaries before the shape transformation possess a triangular cross-sectional profile with a 1.26 μm base width and a 3.4 μm height. Despite the residence times of C460 and P597 in triangular capillaries comparable to those in 500 nm-radius capillaries, the resolution is much lower (R_s = 2.4), which is due to the reduced effective surface area accessible to the species in a triangular geometry.

Figure 3b presents the van Deemter plots from the respective chromatograms obtained under a separation pressure ranging from 20 to 100 psi. The reduced plate height h is the plate height H normalized by the critical channel/capillary size d_c (the capillary diameter or the slit depth) and the reduced linear velocity υ is the linear mobile phase velocity U normalized by D_i/d_c, with D_i the diffusivity of the solutes in the mobile phase. The velocity U is estimated as the zone velocity of the nonretentive species (P597). For the triangular profile, d_c is set to 1 μm, the diameter of the inscribed circle. The D_i coefficients are set based on the measurements taken directly in 500 nm capillaries as 1278 ± 22 and 1044 ± 51 $\mu m^2\ s^{-1}$ ($n = 6$) for P597 and C460, respectively (Figure S-6). In the plots, theoretical curves are also included based on the definition of the plate height $H = 2D_i^*/U$, where dispersion is given by $D_i^* = D_i + f(Ud_c)^2/210D_i$, with f being determined by the channel geometry; typically ~1.1 for a cylindrical or a triangular profile and ~5 for a rectangular profile at an aspect ratio (depth/height) of 0.28.[33,34] Then the reduced plate height is given as $h = B/\upsilon + C\upsilon$, with B being 2 irrespective of the channel geometry and C being $f/105$, a constant specific to the channel geometry. The B term represents longitudinal diffusion and dominates the equation here such that the C term representing the resistance to the transverse mass transfer can be ignored. For the range of velocities presented, the curves can be described by a single equation $h \sim 2/\upsilon$ and return reasonable fittings for nanoslits and narrow capillaries, but mostly underestimate the experimental plate heights for wide capillaries for reasons unclear at present.

The minimum plate heights achieved across all the channel geometries fall mostly below 2.5 μm but above 1.2 μm on average and correspond to 400000 and 833000 plates/m, respectively. The values obtained with 300 nm radius capillaries are typically lower than those with 750 nm slits by about 0.5 μm owing to the slightly higher mobile phase velocity of these capillaries at the maximum applied pressure (100 psi). Likewise, the relatively high mobile phase velocities of the triangular as well as 500 nm radius capillaries, owing to their low hydrodynamic resistances, reduce the minimum plate heights of the nonretentive species (P597) below ~1.5 μm on average but do not alter those of the retentive species (C460), which remain around 2.5 μm. These values are comparable, if not better than those reported for the nanochannels fabricated by e-beam lithography (for benchmarking against state of the art in all four LC modes, see text and Table S-2 in Supporting Information).[25] However, the values are considerably larger than the minimum plate height values theoretically achievable, $h_{\min} = 2\sqrt{BC}$, at an optimal reduced velocity, $\upsilon_m = \sqrt{B/C}$, which are predicted to be around 0.6 μm ($\upsilon_m \sim 6.5$) for nanoslits and triangular capillaries and 0.3 μm ($\upsilon_m \sim 14$) for cylindrical capillaries.

Ion-valence LC. This mode of chromatography, which we refer to as ion-valence LC, relies on the uneven distribution of ionic species across the channel due to transverse electromigration of such species within EDLs of the channel walls based on their valence.[16,22] Under a pressure-driven flow, the species closer to the center streamline are driven faster than those concentrated near the channel walls (the low-speed region) due to the parabolic velocity profile of the laminar streams. That is, ionic species travel along the channel at an axial mean speed that depends on their valence and their consequent spatial distribution across the channel. This forms the basis of the species fractionation in this chromatography mode, which is far more effective in nanochannels than in microchannels because EDLs in such conduits influence a greater portion of the fluid content at a given low-ionic strength.[18]

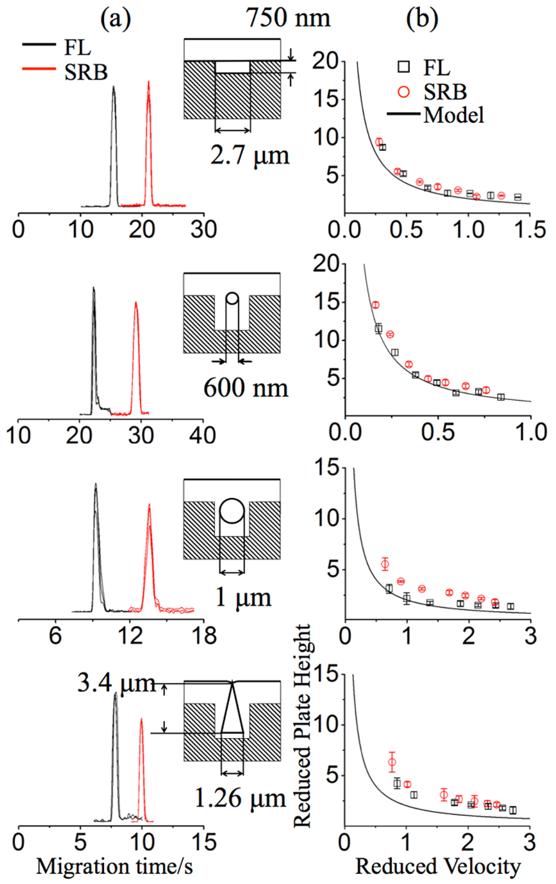

Figure 4. Ion-valence LC. (a) Overlaid chromatograms of SRB and FL (3 repeats) in 100 μM sodium tetraborate buffer (pH ~ 8.9) separated through nanoslits or self-enclosed nanocapillaries of respective cross-sectional profiles (insets). (b) Corresponding reduced van Deemter curves. Error bars: ±1 s.d. ($n = 5$). The model lines represent $h = B/\upsilon + C\upsilon$, where B and C values are as previously stated. Separation length and pressure: 10 mm; (a) 40 and (b) 20−100 psi.

Figure 4 shows the chromatograms of fluorescein (FL) and sulforhodamine B (SRB) associated with respective channel geometries (three repeats at a separation pressure of 40 psi). The binary mixture of anionic species is fully resolved in all channel geometries owing to the small channel width in relation to the thickness of EDLs ~ 30.4 nm (100 μM sodium tetraborate, pH ~ 8.9). At this pH, the channel walls are all negatively charged and this forces FL (−2 charged) more tightly focused along the center streamline than SRB (−1 charged). Consequently, the FL band travels at a higher mean axial speed than the SRB band. In comparison, the resolution trend in this chromatography mode deviates from the presented for the normal-phase LC: 300 nm radius self-enclosed capillaries show no obvious advantage over 750 nm deep nanoslits ($R_s \sim 5.7$ for both geometries) but do offer benefit over 500 nm radius capillaries ($R_s \sim 3.5$). This might be at first attributed to the large residence time in narrow capillaries. Nevertheless, when a comparably low residence time is attained through an increased separation pressure (100 psi), the resolution in narrow capillaries becomes even further enhanced ($R_s \sim 10.5$, Figure S-5b). Alternatively, shifting the detection zone to the nanocapillary upstream without altering the separation pressure (40 psi), as implemented before, delivers a similar residence time and excludes any potential gain from a high separation pressure; the resolution drops slightly ($R_s \sim 5$, Figure S-5c) and yet still exceeds the resolving power of 500 nm radius capillaries. The results suggest that, in this mode of separation, the channel geometry (slit vs cylinder) is not as critical as the channel dimension (slit half-height or capillary radius). However, one should also take into consideration the effective channel geometry wherein sharp corners can be masked by the rounding-off effect of the overlapping large EDLs. The resolution obtained with a triangular geometry ($R_s \sim 2.9$) falls slightly below that of 500 nm radius capillaries, despite the comparable residence times. These results confirm the predictions of previous theoretical studies.[16,17]

The van Deemter plots derived from the chromatograms show similar trends to the plots of the normal-phase LC; the theoretical curves ($h \sim 2/\upsilon$) underestimate the reduced plate heights of the peaks experimentally obtained from wide capillaries while offering a comparatively better fitting to those from nanoslits and 300 nm radius capillaries. Here, the linear mobile phase velocity, U, is taken as the zone velocity of neutral charged species (rhodamine B) independently run in the nanochannels under identical experimental protocols (see Figure S-7 for the plots of U against ΔP, backpressure, where the inverse slopes of the linear fittings give the hydraulic resistances). The diffusion coefficients (D_i) of FL and SRB are set as 425 and 470 μm^2 s^{-1}, respectively.[35] In comparison to the normal-phase LC, this chromatography mode exhibits relatively sharp peaks possibly due to the reduced axial dispersion that comes with the species being confined to the fast streamlines and also comparatively low diffusivity of the ionic species. The minimum plate heights of FL and SRB remain below ~2 μm (the maximum number of plates on average ≥500000 plates/m), except ~2.5 μm for the SRB peak associated with triangular capillaries.

Figure 5 further analyzes the experimental results obtained along 300 and 500 nm radius capillaries filled with separation buffers of various ionic strengths. These results are presented in plots as a function of the normalized capillary radius, κa, where κ and a denote the inverse Debye screening length and the capillary radius, respectively. The resolution data from both capillaries collapse into a single curve with a plateau region ($R_s \sim 5$) extending until a critical radius ($\kappa a \sim 10$) and with a region of rapid decline thereafter (Figure 5a). These results are in good agreement with the results of a previous theoretical study that predicted the optimal channel size as $1 < \kappa a < 10$.[18] In the case of 100 μM sodium tetraborate buffer, κ is about 0.03 nm^{-1}, and the optimal capillary radius for the maximum resolution covers a range from 300 nm down to 30 nm. As expected, increasing κa for a given capillary radius (i.e., increasing κ) reduces the axial migration rate of anionic species, which is more pronounced for FL than SRB, owing to the greater valence and thus more effective electromigration of the former (Figure 5b). An order of magnitude increase in κa leads to a reduction in the axial speed of SRB only ~14%, regardless of the capillary radius, whereas the corresponding reduction for FL is nearly 50% and 29% in 500 nm and 300 nm radius capillaries, respectively. This capillary radius dependence in the case of FL arises from a more effective transverse electromigration of FL than SRB as well as a greater velocity gradient exerted near the walls of wide capillaries than of narrow capillaries.

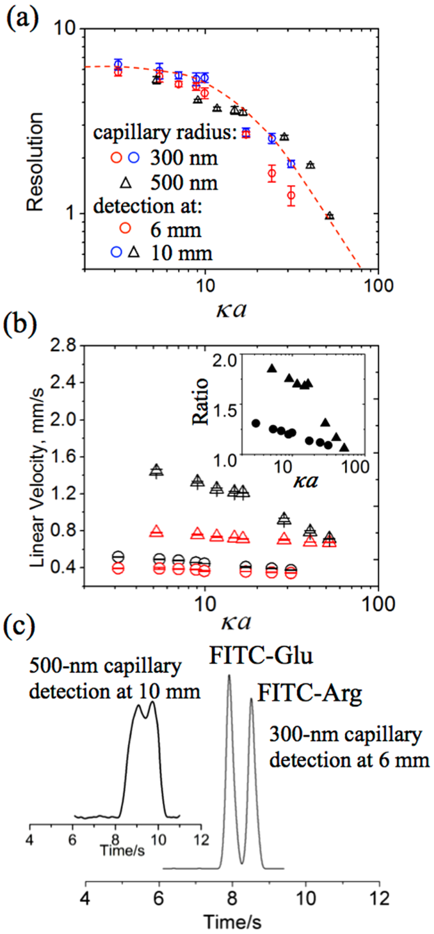

Figure 5. Plots of (a) the resolution and (b) the linear velocity of FL and SRB bands as a function of the normalized capillary radius, κa and (c) the chromatograms of FITC-Glu and FITC-Arg in 100 μM sodium tetraborate buffer (pH 8.9) fractionated based on charge along 300 and 500 nm radius capillaries after a separation run 6 and 10 mm, respectively. In (b), the symbol shape and color denote the capillary radius (triangle: 500 nm; circle: 300 nm) and the species (black: FL; red: SRB), respectively. The inset plot in (b) indicates the ratio of the linear migration velocities of FL to SRB within the same nanocapillaries (triangle: 500 nm; circle: 300 nm). Separation pressure: 40 psi. Error bars: ±1 s.d. (n = 5).

Lastly, the fractionation of anionic (FITC-Glu) and cationic (FITC-Arg) amino acids has been investigated. The mixture, while being unable to resolve after a 10 mm run along 500 nm radius capillaries, are fully resolved into sharp peaks after a 6 mm run along 300 nm radius capillaries within 10 s (Figure 5c). FITC-Glu is repelled from the negatively charged capillary walls and thus exhibits a smaller retention time than FITC-Arg, which is attracted by the walls and travels in comparatively low-velocity streamlines.

Reversed-Phase LC. In this chromatography mode, the solute molecules are separated on the basis of hydrophobicity through a hydrophobic stationary phase and an aqueous mobile phase. The required stationary phase is typically achieved by coating silica surface with a hydrophobic ligand, that is, the sorbent. The reversed-phase LC has been demonstrated here on the fractionation of FITC-labeled amino acids through the nanoslits/nanocapillaries being covalently modified with C18 side chains. Figure 6a shows the chromatograms obtained under isocratic buffer conditions from 500 nm radius capillaries each featuring a set of successfully resolved amino acids: serine, alanine, and proline; and valine, leucine, and phenylalanine, using the elution buffer at an acetonitrile content of 12 and 25%, respectively. Table 1 lists the performance metrics of each amino acid peak. The plate heights obtained are below 5 μm with the lowest value 1.6 μm (617000 plates/m) corresponding to alanine, the only truly resolved peak and, thus, the metrics

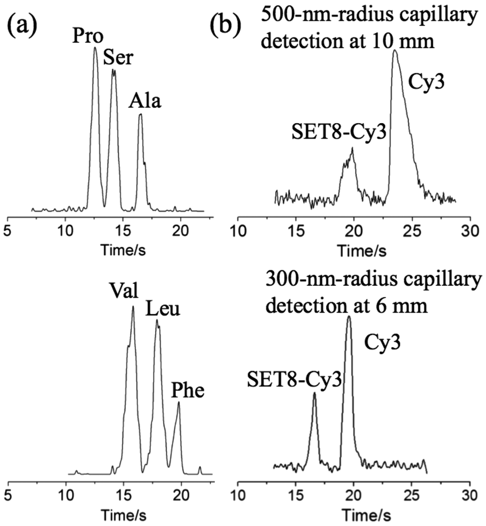

Figure 6. (a) Reversed-phase and (b) hydrodynamic LC. (a) Chromatograms of amino acids in 10 mM citrate buffer (pH 5.5) with 10 mM $NaClO_4$ and acetonitrile (ACN) 12% (the upper plot) and 25% (the lower plot) from a 10 mm separation run along 500 nm radius capillaries modified with C18 side chains on the wall surface. (b) Chromatograms of a mixture of an unreacted free dye (Cy3) and Cy3-labeled protein (SET8) in 1× PBS (pH 7.4) from a separation run 10 and 6 mm along 500 nm and 300 nm radius capillaries, respectively. Separation pressure: 40 psi.

Table 1. Reversed-Phase LC Performance Metrics (Figure 6a)

	Pro	Ser	Ala	Val	Leu	Phe
N (plates)	2041	2388	6114	2401	4344	3353
H (μm)	4.9	4.2	1.6	4.1	2.3	3.0

for which can be independently verified through the method of moments (Supporting Information). The method, however, returns the plate height and number as 5.1 μm and 1951, which are believed to be more representative because of the inaccurate Gauss fit ($R^2 \sim 0.904$) associated with the former values. These metrics somewhat fall behind those reported for silica channels integrated through e-beam lithography, which could be due to the large gap in pressure gradient levels applied along the conduits (Table S-2).[36] The order of elution of the amino acids is in agreement with their hydrophobicity index.[37] In comparison, the chromatograms obtained from 750 nm deep nanoslits return lower resolutions, whereas those from triangular capillaries feature peaks fused together except for the peak of alanine (Figure S-8). Apparently, the chromatograms from 300 nm radius capillaries could not be obtained despite repeated attempts due to clogging associated with the coating procedure.

Hydrodynamic LC. In nanochannels, analytes with large hydrodynamic radii are excluded from the channel walls and thus unable to sample low velocity streamlines near the walls. Consequently, these analytes travel faster than those with smaller hydrodynamic radii.[38] This method has been applied here to the removal of unbound free dye from the fluorescent conjugate, which is a crucial step in the fluorescent labeling macromolecules and nanoparticles.[39] Efficient purification of the fluorescent conjugate is essential to accurately determine the molar ratio of dye to target and to ensure a low fluorescent background during single-molecule imaging. This preparative step is often realized through extensive dialysis, spin-column centrifugation, and gel filtration.[40]

Figure 6b shows the chromatograms of unreacted Cy3 and Cy3-labeled SET8 protein resolved along 300 nm and 500 nm radius capillaries at an elution pressure of 40 psi. The SET8 is a recently discovered single subunit enzyme that prefers nucleosomal substrates and specifically methylates nucleosomal histone H4 at lysine 20.[41] The unreacted dye is fully resolved from the dye-conjugated protein along the capillaries of either size within a comparably short residence time (below 30 s); the resolution achieved with narrow capillaries ($R_s \sim 2.6$) is slightly higher than with large capillaries ($R_s \sim 1.9$). The latter is comparable to the value obtained with the nanoslits ($R_s \sim 1.8$), while the peaks being unable to fully resolve along triangular capillaries (Figure S-9). Nevertheless, these results cannot be explained by hydrodynamic chromatography alone because hardly any separation can be expected for the aspect ratio λ (the ratio of the analyte size to the capillary diameter) below 0.02 according to the simple quadratic model.[37] The SET8 protein is about 5 nm big (MW ∼ 45 kDa) and yet still get resolved in conjugated form from free Cy3 molecules (MW ∼ 767 Da) through 300 nm and 500 nm radius capillaries, especially along such a short separation length (10 mm; $\lambda < 0.01$). Typical theoretical plate numbers are in the order of 10^5 plates/m and the corresponding minimum plate heights are ≤ 1.5 μm for the peak pair resolved in 300 nm radius capillaries, as opposed to ≥ 4.4 μm for the peak pair resolved in 500 nm radius capillaries.

To explain this unexpected outcome, we consider additional mechanisms such as hydrophilic and charge-based interactions between the species and the glass capillary wall; the latter concerns, however, only those species that remain in direct contact with the capillary wall ($\kappa^{-1} < 1$ nm for 1× PBS; pH 7.4). At this high ionic strength, the capillary wall EDLs are ineffective to redistribute the charged species within the capillary to engage ion-valence LC. Further experiments at various pH levels (see text and Figure S-10 in Supporting Information) suggest contributions from two factors: (1) a pH-dependent affinity of Cy3 to the silica surface and (2) a rapid differential removal of Cy3-labeled proteins from the surface by an effective hydrodynamic drag owing to their large molecule size. However, further investigation is needed to reveal the true mechanism.

■ CONCLUSION

We have presented experimental results on pressure-driven chromatography from self-enclosed integrated nanocapillaries with the fabrication technique and the structure distinct from known nanochannels. The nanocapillaries are silica-based robust constructs and integrated through well-established methods without the requirement of advanced patterning or exotic fabrication techniques. These results provide the first experimental account of chromatographic characteristics of integrated nanocapillaries in cylindrical and triangular cross-sectional profiles in relation to those of conventional nanoslits. The resolving power obtained with cylindrical nanocapillaries is generally higher than those with triangular nanocapillaries and conventional nanoslits. In ion-valence chromatography, the solutes that cannot be separated through 500 nm radius capillaries can be fully resolved through 300 nm radius capillaries under the same elution pressure after a comparatively short separation run. The latter radius coincides with the upper size limit predicted for a maximum separation resolution at the

DOI: 10.1021/acs.analchem.6b03094
Anal. Chem. 2016, 88, 11601−11608

stated κ^{-1}; hence, our results in part validate previous theoretical analyses.

The van Deemter curves are found in excellent agreement with the plate heights theoretically predicted for 750 nm deep nanoslists and 300 nm radius capillaries. The minimum plate heights achieved (often less than 2 μm) are still greater than the theoretically expected values. Thus, with a further increase in the elution pressure, the separation performance can be enhanced by an order of magnitude to the levels of 10^6 plates/m. The robust self-enclosed nanocapillaries demonstrated here by leveraging well established microfabrication techniques could advance microsystems toward a high-performance liquid chromatographic analysis of extremely low-volume samples (e.g., single-cell lysate).

■ ASSOCIATED CONTENT

Ⓢ Supporting Information

The Supporting Information is available free of charge on the ACS Publications website at DOI: 10.1021/acs.analchem.6b03094.

> Additional information as noted in text. Device fabrication; pneumatic system; the method of moments; further results and discussion on hydrodynamic LC; benchmarking analysis; supplementary figures and tables (PDF).

■ AUTHOR INFORMATION

Corresponding Author

*Phone: +852-2358 7068. Fax: +852-2358 1485. E-mail: eelyobas@ust.hk.

Notes

The authors declare no competing financial interest.

■ ACKNOWLEDGMENTS

This project was financially supported by the Research Grant Council of Hong Kong under Grant 621513. The authors thank Dr. Hyokeun Park for providing SET8 protein.

■ ABBREVIATIONS

ACN, acetonitrile; Ala, alanine; Arg, arginine; C460, coumarin 460; COMOSS, collocated monolith support structures; DRIE, deep reactive ion etching; EDLs, electric double layers; EKSIV, electrokinetic separation by ion valences; FITC, fluoresciene-5-isothiocyanate; FL, fluorescein; Glu, glutamic acid; LC, liquid chromatography; Leu, leucine; LPCVD, low-pressure chemical vapor deposition; MW, molecular weight; PBS, phosphate buffered saline; Phe, phenylalanine; Pro, proline; P597, pyrromethene 597; PSG, phosphosilicate glass; SEM, scanning electron microscopy; Ser, serine; SRB, sulforhodamine B; Val, valine

■ REFERENCES

(1) Tsukahara, T.; Mawatari, K.; Kitamori, T. *Chem. Soc. Rev.* **2010**, *39*, 1000−1013.

(2) Sparreboom, W.; van den Berg, A.; Eijkel, J. C. T. *Nat. Nanotechnol.* **2009**, *4*, 713−720.

(3) Wang, D. J.; Bodovitz, S. *Trends Biotechnol.* **2010**, *28*, 281−290.

(4) Hibara, A.; Saito, T.; Kim, H. B.; Tokeshi, M.; Ooi, T.; Nakao, M.; Kitamori, T. *Anal. Chem.* **2002**, *74*, 6170−6176.

(5) Tsukahara, T.; Hibara, A.; Ikeda, Y.; Kitamori, T. *Angew. Chem., Int. Ed.* **2007**, *46*, 1180−1183.

(6) Pu, Q. S.; Yun, J. S.; Temkin, H.; Liu, S. R. *Nano Lett.* **2004**, *4*, 1099−1103.

(7) Rice, C. L.; Whitehead, R. *J. Phys. Chem.* **1965**, *69*, 4017−4024.

(8) Kobayashi, Y.; Martin, C. R. *Anal. Chem.* **1999**, *71*, 3665−3672.

(9) Tas, N. R.; Mela, P.; Kramer, T.; Berenschot, J. W.; van den Berg, A. *Nano Lett.* **2003**, *3*, 1537−1540.

(10) Han, J.; Craighead, H. G. *Science* **2000**, *288*, 1026−1029.

(11) Peterson, N. J.; Alarie, J. P.; Jacobson, S. C.; Ramsey, J. M. *Proc. 7th Int. Conf. Miniaturized Chem. Biochem. Anal. Syst. 2003*, Squaw Valley, CA, Kluwer Academic: New York, 2003; Vol. *1*, pp 701−703.

(12) Pennathur, S.; Baldessari, F.; Santiago, J. G.; Kattah, M. G.; Steinman, J. B.; Utz, P. J. *Anal. Chem.* **2007**, *79*, 8316−8322.

(13) Pennathur, S.; Santiago, J. G. *Anal. Chem.* **2005**, *77*, 6772−6781.

(14) Pennathur, S.; Santiago, J. G. *Anal. Chem.* **2005**, *77*, 6782−6789.

(15) Garcia, A. L.; Ista, L. K.; Petsev, D. N.; O'Brien, M. J.; Bisong, P.; Mammoli, A. A.; Brueck, S. R. J.; Lopez, G. P. *Lab Chip* **2005**, *5*, 1271−1276.

(16) Griffiths, S. K.; Nilson, R. H. *Anal. Chem.* **2006**, *78*, 8134−8141.

(17) Xuan, X. C.; Li, D. Q. *Electrophoresis* **2007**, *28*, 627−634.

(18) Xuan, X. C. *Electrophoresis* **2008**, *29*, 3737−3743.

(19) Jung, S.; Höltzel, A.; Ehlert, S.; Mora, J.-A.; Kraiczek, K.; Dittman, M.; Rozing, G. P.; Tallarek, U. *Anal. Chem.* **2009**, *81*, 10193−10200.

(20) He, B.; Tait, N.; Regnier, F. *Anal. Chem.* **1998**, *70*, 3790−3797.

(21) Knox, J. H. *J. Chromatogr. Sci.* **1980**, *18*, 453−461.

(22) Wang, X. Y.; Kang, J. Z.; Wang, S. L.; Lu, J. J.; Liu, S. R. *J. Chromatogr., A* **2008**, *1200*, 108−113.

(23) Wang, X. Y.; Cheng, C.; Wang, S. L.; Zhao, M. P.; Dasgupta, P. K.; Liu, S. R. *Anal. Chem.* **2009**, *81*, 7428−7435.

(24) Wang, X. Y.; Liu, L.; Pu, Q. S.; Zhu, Z. F.; Guo, G. S.; Zhong, H.; Liu, S. R. *J. Am. Chem. Soc.* **2012**, *134*, 7400−7405.

(25) Ishibashi, R.; Mawatari, K.; Kitamori, T. *Small* **2012**, *8*, 1237−1242.

(26) Kato, M.; Inaba, M.; Tsukahara, T.; Mawatari, K.; Hibara, A.; Kitamori, T. *Anal. Chem.* **2010**, *82*, 543−547.

(27) Xu, Y.; Wang, C. X.; Li, L. X.; Matsumoto, N.; Jang, K.; Dong, Y. Y.; Mawatari, K.; Suga, T.; Kitamori, T. *Lab Chip* **2013**, *13*, 1048−1052.

(28) Liu, Y. F.; Yobas, L. *Biomicrofluidics* **2012**, *6*, 046502.

(29) Cao, Z.; Yobas, L. *Anal. Chem.* **2014**, *86*, 737−743.

(30) Cao, Z.; Yobas, L. *ACS Nano* **2015**, *9*, 427−435.

(31) Tang, J.; Du, N.; Doyle, P. S. *Proc. Natl. Acad. Sci. U. S. A.* **2011**, *108*, 16153−16158.

(32) Sukas, S.; De Malsche, W.; Desmet, G.; Gardeniers, H. J. G. E. *Anal. Chem.* **2012**, *84*, 9996−10004.

(33) Dutta, D.; Leighton, D. T. *Anal. Chem.* **2001**, *73*, 504−513.

(34) Ajdari, A.; Bontoux, N.; Stone, H. A. *Anal. Chem.* **2006**, *78*, 387−392.

(35) Culbertson, C. T.; Jacobson, S. C.; Ramsey, J. M. *Talanta* **2002**, *56*, 365−373.

(36) Smirnova, A.; Shimizu, H.; Mawatari, K.; Kitamori, T. *J. Chromatogr., A* **2015**, *1418*, 224−227.

(37) Monera, O. D.; Sereda, T. J.; Zhou, N. E.; Kay, C. M.; Hodges, R. S. *J. Pept. Sci.* **1995**, *1*, 319−328.

(38) Tijssen, R.; Bos, J.; Vankreveld, M. E. *Anal. Chem.* **1986**, *58*, 3036−3044.

(39) Tenuta, T.; Monopoli, M. P.; Kim, J. A.; Salvati, A.; Dawson, K. A.; Sandin, P.; Lynch, I. *PLoS One* **2011**, *6*, e25556.

(40) Brinkley, M. *Bioconjugate Chem.* **1992**, *3*, 2−13.

(41) Fang, J.; Feng, Q.; Ketel, C. S.; Wang, H. B.; Cao, R.; Xia, L.; Erdjument-Bromage, H.; Tempst, P.; Simon, J. A.; Zhang, Y. *Curr. Biol.* **2002**, *12*, 1086−1099.